JACS
JOURNAL OF THE AMERICAN CHEMICAL SOCIETY

ARTICLE

pubs.acs.org/JACS

Electrogenerated Chemiluminescence of Conjugated Polymer Films from Patterned Electrodes

Song Guo,*[,†] Omar Fabian,[‡] Ya-Lan Chang,[†] Jiun-Tai Chen,[†,§] William M. Lackowski,[†] and Paul F. Barbara[†,∥]

[†]Department of Chemistry and Biochemistry and Center for Nano and Molecular Science and Technology, University of Texas at Austin, Austin, Texas 78712, United States

[‡]Materials Science and Engineering Program, University of Texas at Austin, Austin, Texas 78712, United States

[§]Department of Applied Chemistry, National Chiao Tung University, Hsinchu, Taiwan 30050

Supporting Information

ABSTRACT: A new phenomenon is presented in which electrogenerated chemiluminescence (ECL) is generated and propagates laterally as self-reinforcing waves as a result of the oxidation of a poly(9,9-dioctylfluorene-*co*-benzothiadiazole) thin film. In an ordered array of Au electrode posts that act as effective ECL nucleation sites, soliton-like waves were observed to expand from each site and annihilate upon collision with each other. Simulations of the ECL response supported the experimental observations that the ECL waves propagate at a constant speed. A correlated diffusion mechanism involving the correlated motion of ions, injected holes, and solvent molecules is proposed to interpret the experimental data qualitatively. A rapid increase in the diffusion coefficient of these species in the polymer results in a sharp interface between non-oxidized and oxidized polymer phases wherein the electrochemical (EC) oxidation and mass transport of all pertinent species take place. EC oxidation of conjugated polymers of this type has important implications for the understanding of these materials and their modes of operation in EC conjugated polymer devices.

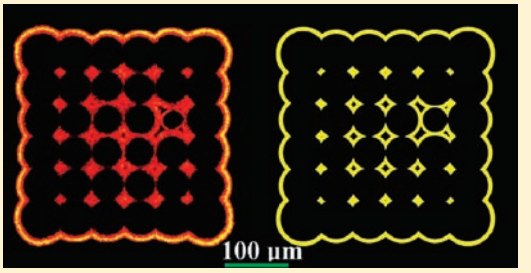

INTRODUCTION

The understanding of oxidation and reduction processes in active materials is crucial for the successful implementation of electrochemical (EC) conjugated polymer devices, including electrochemical light-emitting diodes,[1] thin-film sensors,[2,3] electrochromic window coatings,[4,5] and electrochemical actuators.[6,7] During oxidation and reduction of a polymer film, injected carriers, counterions, and solvent molecules diffuse into the polymer, and several key properties of the material, such as the conductivity, the diffusion coefficient of the species moving through the polymer, the optical properties, and even the mechanical properties, change substantially. An important problem in EC conjugated polymers is understanding the kinetics of these electrochemical processes, which ultimately control the performance and durability of the aforementioned devices.

Previous studies of mass and charge transfer in conjugated polymers during EC oxidation or reduction have mainly been based on the direct observation of electrochemically induced color (RGB) changes. High-resolution optical microscopy studies have shown that the oxidation process in polypyrrole (PPy) propagates with a sharp front.[8−10] Smela and co-workers[11−15] reported that the electrochromic changes in films of PPy doped with dodecyl benzenesulfonate [PPy(DBS)] advance with a well-defined front during the first of multiple reduction cycles. However, the propagation of this front during the initial reduction cycle was not a focus of their studies, as they concentrated strictly on the lateral transport of ions in thin films subjected to several reduction cycles and reported a migration-dominated transport mechanism with wave velocities scaling linearly with the applied potential. They also demonstrated that the thickness of PPy(DBS) films increases substantially during reduction as a result of swelling. Otero and co-workers[16−19] reported that oxidized regions propagate as waves in PPy films and hypothesized that oxidation propagation in conjugated polymers proceeds via a chain-relaxation process that serves as the rate-limiting step in their proposed electrochemically stimulated chain relaxation (ESCR) model.

Alternatively, studies conducted in our laboratory have utilized electrogenerated chemiluminescence (ECL) reactions to monitor EC oxidation processes.[20,21] On the basis of our previous studies, photoluminescence (PL) and ECL measurements from an unoxidized polymer film are distinct from those of an oxidized polymer film.[22] On the contrary, electrochromic changes are reversible and may even be indistinguishable in multiple oxidation cycles performed on a single film. Also, because ECL is the only light signal detected during an experiment, a better signal-to-noise ratio relative to that for monitoring of electrochromic changes is achieved. This makes ECL a better probe for investigating certain property changes in polymer films. In particular, it

Received: January 6, 2011
Published: June 24, 2011

provides essential information on the EC oxidation process at a very early stage, to which previous methods are less sensitive. It is important to note that our studies focus on electrochemical processes following a single oxidation step, which is not only necessary to reliably and reproducibly quantify the propagation of oxidation waves but also relevant for understanding the break-in mechanism of EC conjugated polymer devices.[14,23]

ECL has been observed to initiate and propagate laterally within spin-coated conjugated polymer thin films in the form of soliton-like waves.[22] A polymer film is oxidized after an ECL wave passes through it, and to date, the mechanism of ECL wave propagation has remained unclear. The diffusion of ions, injected holes, and solvent molecules in thin polymer films are critical steps in the ECL wave propagation process. In our previous studies, the triggering sites for ECL waves were spontaneously formed defects or randomly dispersed Au nanoparticles in polymer films.[22] The uncertainty in the location of these sites, arising from random positions, irregular shapes, and size dispersion, led to uncertainty in determining the properties of the produced ECL waves. The development of a better way to control the initiation of ECL waves is imperative for gaining a deeper understanding of the EC oxidation mechanism and its potential applications.[24,25]

Here we report ECL waves in spin-coated poly(9,9-dioctylfluorene-*co*-benzothiadiazole) (F8BT) thin films (~250 nm) in contact with Au patterned electrodes. Using electron-beam lithography (EBL), Au patterns such as posts and bars were precisely grown on indium tin oxide (ITO) substrates, and ECL waves were observed to launch from each Au electrode. A simple constant-wave-speed simulation matched the ECL waves observed from optical micrographs very well. Furthermore, an ionic cluster diffusion mechanism is proposed to describe the mass transport within the polymer film during ECL wave propagation. Qualitative modeling of this mechanism produced the main characteristics of the ECL waves observed from the fabricated Au pattern.

EXPERIMENTAL SECTION

Fabrication of Au Posts. A 300 μL solution of 9 wt % PMMA in chlorobenzene (MicroChem, 950k PMMA C9) was spin-coated onto a cleaned ITO-patterned glass substrate at 3000 rpm for 60 s to form a photoresist layer with a thickness of ~1.8 μm. The sample was then baked on a hot plate at 373 K for 20 min. Electron-beam irradiation was carried out using a Reith50 EBL system (Reith GmbH) to pattern-etch the photoresist. The exposed sample was developed in a 1:3 methyl isobutyl ketone (MIBK)/isopropyl alcohol (IPA) solution for 60 s and then rinsed in IPA solution for 60 s. A 20 nm Cr layer and a 50−400 nm Au layer were thermally evaporated onto the sample. Finally, the sample was immersed in acetone overnight to remove the photoresist layer and the metal above it. An illustration of the fabrication process is shown in Figure S1 in the Supporting Information.

ECL Studies. F8BT (140 kg/mol) was purchased from American Dye Source. Lithium perchlorate ($LiClO_4$, 99.99%) and tri-*n*-propylamine (TPA-H, 99+%) were obtained from Sigma-Aldrich. Acetonitrile (MeCN, 99.9%) was obtained from AcroSeal and toluene (extra dry, water <30 ppm) from Acros. A 150 μL F8BT/toluene solution (28 mg/mL) was spin-coated onto a Au-patterned ITO substrate to form a ~220 nm F8BT film. An electrochemical cell was built directly on the polymer film and filled with an MeCN solution containing 0.1 M $LiClO_4$ and 0.1 M TPA-H. The applied EC potential reported here was measured relative to a silver-wire quasi-reference electrode (QRE). The potential was controlled and recorded by a PGSTAT100 potentiostat (Metrohm Autolab). Au-coated glass coverslips were used as counter electrodes (CEs). The potential relative to the QRE was 0.20 ± 0.04 V vs the ferrocene/ferrocenium (Fc/Fc^+) couple. ECL micrographs were acquired using a wide-field optical microscope (Nikon, Eclipse TE2000) equipped with a charge-coupled device (CCD) camera (Roper Scientific, Cascade 512B).

RESULTS AND DISCUSSION

Figure 1 shows a schematic of the electrochemical cell along with a transmission image of an F8BT-coated ITO substrate with a Au post acting as a ECL nucleation site (trigger). The Au post was lithographically fabricated on the ITO substrate and is represented by the black dot in Figure 1a. The height of the Au post (370 nm) was much higher than the thickness of the F8BT film (~220 nm). It is very likely that after spin-coating, the Au post protruded through the polymer film. This configuration was tantamount to having an extended working electrode (WE) on the top surface of the polymer film. Previous work has shown that with an applied electrochemical potential, the electrical double layer required for the electrochemical reaction forms at the interface between the solution, the polymer film, and the WE.[21,22] The double layer initiates the oxidation of the polymer film, which is the first step of the light-emitting ECL reaction:[21,26]

$$\mathrm{F8BT} - \mathrm{e}^- \rightarrow \mathrm{F8BT}^{+\bullet} \quad (1)$$

The injected holes are transported to the top layer of the oxidized polymer, where they react with TPA-H, the co-reactant for the ECL reaction in the electrolyte solution:

$$\mathrm{F8BT}^{+\bullet}(\text{at double layer}) \rightarrow \mathrm{F8BT}^{+\bullet}(\text{at polymer}-\text{electrolyte interface}) \quad (2)$$

$$\mathrm{TPA\text{-}H} - \mathrm{e}^- \rightarrow [\mathrm{TPA\text{-}H}^{+\bullet}] \rightarrow \mathrm{TPA}^{\bullet} + \mathrm{H}^+ \quad (3)$$

There are two possible schemes for generation of the excited state of F8BT, the first of which is via an electron-transfer step:

$$\mathrm{F8BT}^{+\bullet} + \mathrm{TPA}^{\bullet} \rightarrow \mathrm{F8BT}^* + \mathrm{TPA}^+ \quad (4)$$

The second is via the formation of $F8BT^{-\bullet}$ and its annihilation by $F8BT^{+\bullet}$:

$$\mathrm{F8BT} + \mathrm{TPA}^{\bullet} \rightarrow \mathrm{F8BT}^{-\bullet} + \mathrm{TPA}^+ \quad (5)$$

$$\mathrm{F8BT}^{+\bullet} + \mathrm{F8BT}^{-\bullet} \rightarrow \mathrm{F8BT}^* + \mathrm{F8BT} \quad (6)$$

The excited state of the polymer then emits a photon upon relaxation:

$$\mathrm{F8BT}^* \rightarrow \mathrm{F8BT} + h\nu \quad (7)$$

A series of time-lapse ECL images with an integration time of 100 ms and after the application of a +1.6 V electrochemical potential to the sample is shown in Figure 1b. The figure shows an ECL wave expanding from the Au post isotropically to form a ring. Oxidation of the polymer induces its transition from a nonconducting phase to a conducting phase, accompanied by the swelling of the oxidized polymer phase by charge-compensating anions and solvent molecules. At times beyond this initial oxidation, the conducting polymer phase effectively acts as an extension of the WE, and the oxidation front propagates as a wave. ECL is initiated from the edge of the Au post and expands as a well-defined circular wave. If the height of the Au post were lower than

or comparable to the thickness of the film, the resulting film would likely cover the top of the electrode. The Au electrode would then have no direct exposure to the electrolyte solution, preventing the formation of a double layer and hence the ECL. For example, no ECL waves were detected from any 50 nm Au posts in a 220 nm F8BT film, and for 235 nm Au posts in a 220 nm F8BT film, the triggering probability of an ECL wave was less than 20%.

A series of time-lapse ECL images from a 6 × 6 array of Au posts with heights of 370 nm are displayed in Figure 2. Immediately after a +1.6 V potential step was applied, ECL waves were initiated from every Au post. Each ECL wave propagated isotropically as a well-defined ring, as was previously reported.[22] When neighboring ECL waves collided, their luminescent fronts were annihilated at every point of contact, and the remaining fronts appeared to merge. The speed of the ECL wave fronts did not change immediately before or after the collision, suggesting that the interactions between colliding ECL waves are short-ranged. After 0.8 s, all of the ECL waves inside the array were annihilated, resulting in one merged ECL wave propagating outward as a collectively larger wave with a sharp front.

The experimental results indicate that the ECL waves propagate at a constant speed.[22] However, the annihilation of the ECL wave interiors made direct measurement of the speed of the individual ECL waves difficult at later times. A constant-speed model was used to simulate the ECL waves observed in Figure 2. The flowchart in Figure 3 describes the algorithm used in this model. A ring centered at a given starting point was drawn with a radius calculated as the product of the time (t) and speed (k) parameters. All of the intersecting perimeters of multiple ECL

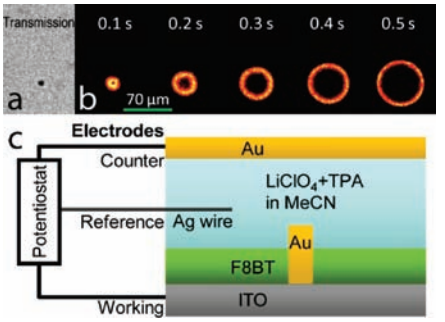

Figure 1. (a) Transmission image of a ~200 nm F8BT film on ITO. A square-shaped, 370 nm tall Au feature was lithographically fabricated on the ITO working electrode (WE). (b) ECL images acquired after a +1.6 V potential step was applied to the WE of the sample shown in (a). (c) Schematic of the electrochemical cell. The electrodes were the following: a silver wire quasi-reference electrode (QRE), a gold planar counter electrode (CE), and a 200 nm F8BT-coated ITO WE.

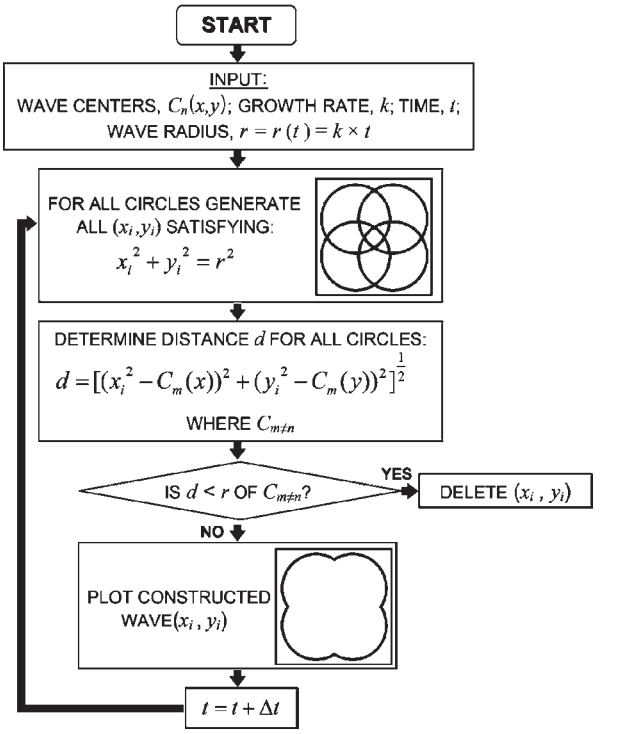

Figure 3. Flowchart showing the algorithm employed to simulate ECL waves emanating from point sources. The initial conditions of the system consist of the arrangement and number of wave centers in space and the constant rate at which the circular waves propagate, which defines the wave radius at a given instant in time. Upon initiating these parameters, the algorithm expands the circular wave radius at the growth rate. When the waves intersect, the portions of the waves' perimeters beginning from the points of contact to their subsequent advances into the interiors of neighboring waves are excised, leaving only the perimeter of the excluded area. The flowchart also illustrates four neighboring waves that have intersected, shown before and after the excision has been applied.

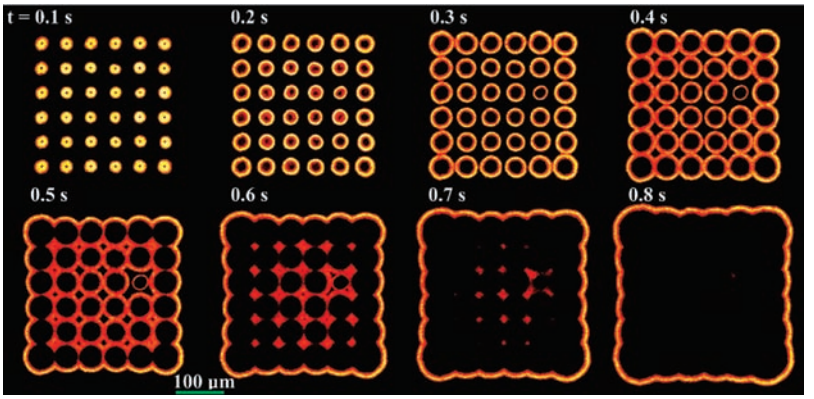

Figure 2. Series of time-lapse ECL images from a ~200 nm F8BT film acquired during a +1.6 V (vs Ag QRE) potential step. The time at which each frame was acquired is shown at the top-left corner of each image. A 6 × 6 array of 5 μm gold squares was lithographically fabricated on the ITO WE; the spacing between the gold posts was 50 μm. ECL waves were initiated from this array of 370 nm tall Au features.

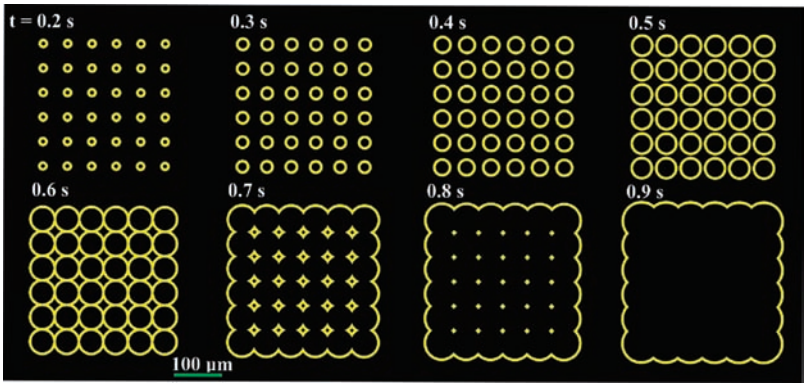

Figure 4. Series of time-lapse simulated ECL waves initiated from a 6 × 6 array with 50 μm spacing between neighboring starting points. The integration time of each frame was 100 ms. The time at which each frame was acquired is shown at the top-left corner of each image. The ECL waves propagate from the starting points at t = 0.0 s with a constant speed of 45 μm/s. The ECL wave fronts are annihilated at all points of mutual contact.

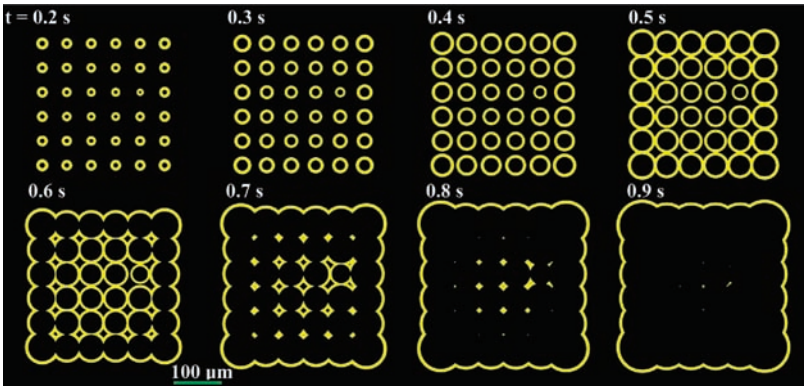

Figure 5. Series of time-lapse simulated ECL waves initiated from a 6 × 6 array with 50 μm spacing between neighboring starting points. The integration time of each frame was 100 ms. The time at which each frame was acquired is shown at the top-left corner of each image. The ECL waves begin propagating from the starting points at t = 0.0 s with a constant speed that varies with the positions of the points. The wave fronts are annihilated when they meet each other.

waves were then removed. The simulation was carried out using time steps finer than the 100 ms steps used in the experiment. The final images were integrated from all of the simulated images within every 100 ms step to provide a better representation of the ECL images observed from the CCD camera in the experiment.

Figure 4 displays simulated images from the constant-speed model for a 6 × 6 array of ECL waves. These images are substantially similar to the experimental data shown in Figure 2. One important detail is that all of the simulated images are delayed by 0.1 s with respect to the corresponding experimental images. This suggests that the initial speeds of ECL waves are higher than their later speeds, which was reported in our previous publication.[22] Unlike the symmetric patterns displayed in the simulated images, the experimental ECL images at 0.6 and 0.7 s show complex geometry at the center of the 6 × 6 array. The main differences between the simulation and the experimental data result from the fact that the speeds of the ECL rings in Figure 2 are not uniform. To account for this nonuniformity, we measured how far each ECL wave traveled within the first 0.3 s and then correspondingly modified the constant speed of each wave in the simulation. The simulated ECL images from the modified model, which are shown in Figure 5, agree well with the experimental data. The 0.1 s delay due to the high initial speed of the wave in the experiment is also observed. In this modified model, the corner ECL waves are always the fastest, followed by those along the outer perimeter, and finally, the inner rings are the slowest. The local ECL wave density might play an important role in this speed variation. One requirement for ECL is the supply of anions (ClO_4^-) from the electrolyte solution.[20,21] The inner ECL waves face more competition for anions, as all neighboring ECL waves require them in order to balance the positive charges of newly injected holes. This establishes a higher local concentration gradient of anions at the corners of the array with respect to those near the center, resulting in the faster diffusion of the waves.

In the 6 × 6 array experiment, one Au post right of center behaved differently from the others. The speed of the ECL wave from this Au post was lower, inducing the complex features shown in the experimental data at 0.6 and 0.7 s in Figure 2. In the modified simulation, the ECL wave from this Au post was given a lower constant speed, and the simulated images at t = 0.7 and 0.8 s matched the complex geometry observed in the experiment. It is very likely that besides the applied potential, the anion concentration, and the TPA-H concentration, the local conditions (e.g., Au post geometry, local defects) at the starting sites of the ECL waves are also very important in determining the ECL

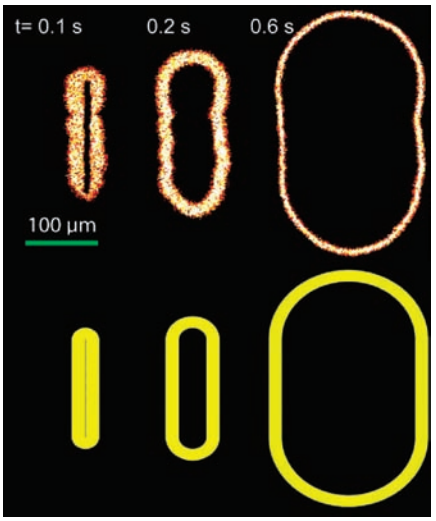

Figure 6. Top row: ECL micrographs of a ~160 nm F8BT film on ITO. A 150 μm × 5 μm gold bar was lithographically fabricated on ITO with a height of 390 nm. The integration time for each micrograph was 100 ms. The time at which each micrograph was acquired after the bias on ITO was stepped from 0.0 to +1.7 V is noted at the top-left corner. Bottom row: simulated ECL image. The ECL wave started from a 150 μm line and propagated freely with a constant speed of 180 μm/s.

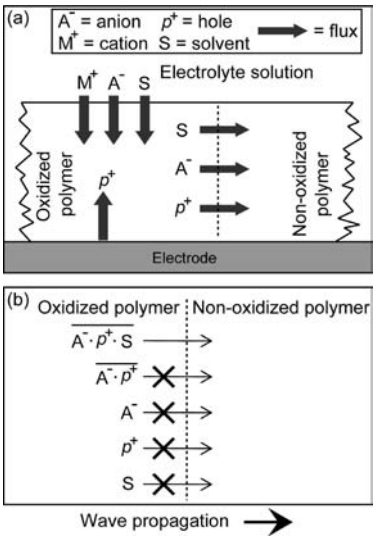

Figure 7. (a) Schematic illustration of the mass transfer of each species into and within the polymer film during the wave propagation process. (b) Possible forms of mass transfer that deliver holes, anions, and solvent molecules from the oxidized to the non-oxidized polymer during wave propagation.

wave speed. Once the ECL wave is established, the speed remains constant, even though neighboring waves propagating in the same film under the same conditions travel at higher speeds.

ECL waves from other Au patterns were also demonstrated. One example is shown in Figure 6, where a 150 μm × 5 μm Au bar with a height of 390 nm was fabricated lithographically on ITO and used as a triggering electrode. ECL images taken after the application of a +1.7 V bias to the ITO WE are displayed in the top row. The ECL wave propagated from the Au bar to form an oval "race-track"-shaped feature. The hemispherical caps at both ends continued to expand, while the straight sections on either side maintained a length equal to that of the bar electrode. The constant-speed model described above produced images matching those in the experiment, as displayed in the bottom row of Figure 6.

When an F8BT film is immersed in the electrolyte solution with no potential applied to the WE, the polymer film remains "dry". If a potential is applied, holes are injected into the film from a positively biased WE to oxidize the polymer.[21,27] Both the injected holes and the electric field inside the film promote the transport of anions into the polymer film. Charge-compensating anions in the electrolyte solution must diffuse into the film to balance the positive charge of the injected holes. Solvent molecules diffuse with anions through the interface between the oxidized polymer film and electrolyte solution. Figure 7 depicts the fluxes of all of the species upon the application of a potential to the WE. While it may be possible for electrolyte cations to diffuse into the polymer film because of their excess concentration in solution, this diffusion mechanism is not electrostatically favorable. It should also be noted that even though the polymer is biased at every point of contact with the ITO WE, any given region of the dry polymer is not electrochemically oxidized until it has been traversed by an oxidation wave, which is visualized by ECL. As an ECL wave propagates across the film, the dry polymer phase becomes oxidized, and the concentrations of anions, injected holes, and solvent molecules increase significantly. This injection of solutes into the "dry" phase has been observed as the "swelling" of polymer films.[22] As the ECL wave propagates away from the electrode, the anions, solvent molecules, and cations from the electrolyte solution may diffuse into the swollen film behind the wave at any point along the interface between the oxidized film and the solution. Holes may also be injected into the swollen film at any point along the interface between the oxidized film and the WE. These fluxes are illustrated in Figure 7a. The lateral fluxes of anions, holes, and solvent molecules from the oxidized to the non-oxidized polymer phase are also shown in Figure 7a.

A complete mathematical treatment of the various processes involved in producing the observed phenomena would require the consideration of all equations pertinent to mass and charge transfer, as discussed in Appendix I in the Supporting Information. Figure 7b shows the different forms of mass transfer for all solute species in the polymer film during the wave propagation process. For an anion−hole pair ($A^- \cdot p^+$) alone to diffuse across the interface between the oxidized and non-oxidized polymer, it must overcome the energy barrier associated with desolvation as it is transferred from the wet region to the dry region. For only anions (A^-) or only holes (p^+) to diffuse, they must overcome a Coulombic energy cost representing the electrostatic unfavorability of having a lone charged species diffuse through the polymer matrix. A desolvation barrier is associated with the diffusion of anion−hole pairs, which also applies to the diffusion of only solvent molecules (S). In principle, the diffusion of a cluster composed of a hole, an anion, and solvent molecules ($A^- \cdot p^+ \cdot S$) would be the most energetically favorable mass transport mechanism, as it involves neither a desolvation barrier nor a Coulombic energy barrier; however, the fact that the non-oxidized polymer film does not swell when immersed in the electrolyte solution suggests that ionic clusters do not diffuse into the non-oxidized region in the absence of an applied electrochemical potential. The lowest-energy pathway is the one that allows the holes, anions, and solvent molecules to diffuse into the non-

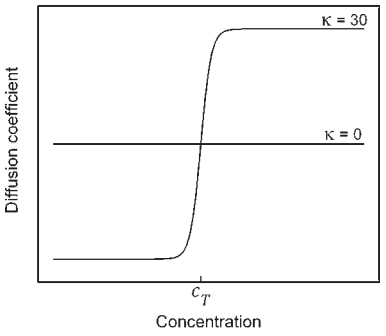

Figure 8. Simulated dependence of the diffusion coefficient (D) on concentration (c) for $\kappa = 0$ and $\kappa = 30$.

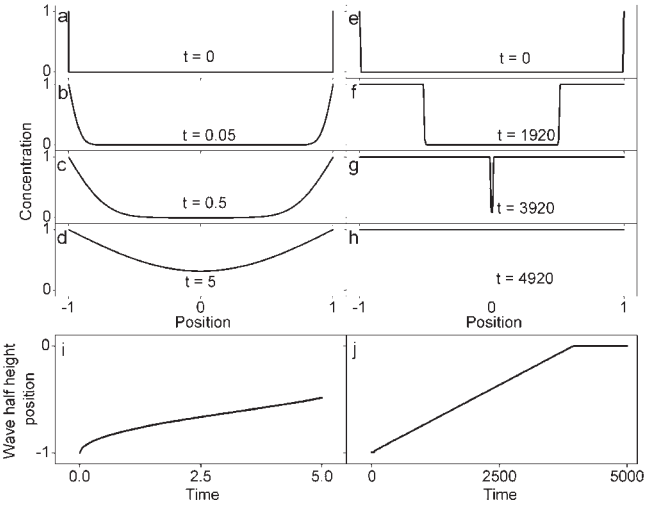

Figure 9. Wave propagation from two ends toward a common point simulated using a diffusion coefficient with a sigmoidal dependence on the ionic cluster concentration inside a polymer film. (a–d) Wave propagation at different times for $\kappa = 0$. (e–h) Wave propagation at different times for $\kappa = 30$. (i) Positions of the half-height of the wave front at different times for the simulation in (a–d). (j) Positions of the half-height of the wave front at different times for the simulation in (e–h).

oxidized polymer in the correlated form of an ionic cluster. On the basis of this ionic cluster model, the diffusion inside the polymer film can be simplified as follows:

$$\frac{c(x, t + \Delta t) - c(x,t)}{\Delta t} = \frac{1}{\Delta x}\left[D(c(x,t))\frac{c(x + \Delta x, t) - c(x,t)}{\Delta x}\right] \quad (8)$$

where c is the concentration of ionic clusters inside the polymer.

The boundary condition here assumes that the ionic cluster reaches a saturated concentration, c_0, at the interface between the polymer, electrode, and electrolyte solution. This saturated concentration is maintained during wave propagation, and therefore,

$$c(-1, t) = 1 \quad \text{and} \quad c(1, t) = 1 \quad (9)$$

where the spatial limits are from −1 to 1 along the x direction. A c value of 1 means that the concentration reaches the saturated value c_0.

A sigmoidal function is employed to express the diffusion coefficient of the ionic cluster, D, inside the polymer as a function of the cluster concentration c, as plotted in Figure 8:

$$D(c) = \frac{D_{wet}}{1 + e^{-\kappa(c - c_T)}} + D_{dry} \quad (10)$$

where D_{wet} and D_{dry} are the diffusion coefficients of the ionic clusters within the wet and dry polymers, respectively, c_T is the concentration at which the diffusion coefficient changes between D_{wet} and D_{dry}, and κ is a parameter that defines how fast the diffusion coefficient changes at the threshold value: when $\kappa = 0$, the diffusion coefficient is independent of the concentration of the ionic clusters. Figure 8 shows how D varies with c for $\kappa = 0$ and $\kappa = 30$.

The initial conditions are as follows:

$$c(x, 0) = 0 \quad (11)$$

$$c_T = 0.95 \quad (12)$$

$$D_{wet} = 10^{-1} \quad (13)$$

$$D_{dry} = 10^{-7} \quad (14)$$

The propagation of concentration waves simulated by the ionic cluster model is shown in Figure 9. When $\kappa = 0$, the shape of the wave front is diffuse and not well defined during propagation. In this case, the diffusion coefficient of the ionic cluster is independent of the cluster concentration, and therefore, the diffusion is purely Fickian. Moreover, the plot of position versus concentration in Figure 9i demonstrates that the wave front moves more slowly as it approaches the center of the simulated space. Figure 9a–d shows only the early stages of wave propagation to emphasize the shape of the wave fronts when $\kappa = 0$. When $\kappa = 30$, as displayed in Figure 9e–h, a diffusion coefficient that is strongly dependent on the ionic cluster concentration produces traveling waves with sharp fronts.[28] In Figure 9g, the two wave fronts maintain their shapes during collision, just as they were observed to do in the ECL experiments. Figure 9j shows that the wave fronts propagate with constant speed until they collide with one another. The simulated wave demonstrates the two main characteristics of ECL waves: a sharp wave front and constant speed. At high κ values (e.g., $\kappa = 30$), when the clusters first begin to diffuse, the diffusion coefficient of the ionic clusters is at its minimum because the cluster concentration is zero in the non-oxidized polymer. Trace amounts of the clusters gradually diffuse to the non-oxidized polymer side, as the diffusion coefficient D still possesses a nonzero value. The buildup of ionic clusters correspondingly results in an increase in D, which further facilitates the accumulation of clusters. As demonstrated in Figure 9f,g, the cluster concentration drops sharply in going from the oxidized polymer to the non-oxidized polymer, leading to a narrow interface between these two phases of the film, which matches the sharp ECL wave front observed in the experiments. This dramatic dependence is likely induced by the electrochemical reactions that take place at the interface and emit luminescence as the reaction front propagates. With the injection of ionic clusters, the polymer becomes swollen.[22] Similar constant wave front speeds were obtained in a theoretical study of non-Fickian diffusion in polymer–solute systems.[29,30]

It should be noted that at this time, this model is empirical and does not take into account such parameters as the electrochemical potential, the anion concentration, and the coreactant concentration nor their effects on ECL wave propagation. A

testament to the limitations of this model is the dependence of the wave propagation speed on the step size of the simulated space, Δx. For example, when $\kappa = 30$, the wave propagation speed appears to continue to increase with the reciprocal of Δx within a reasonable range of step sizes from 1 mm down to 10 nm, as shown in Figure S2 in the Supporting Information. However, if the step size is reduced to a value smaller than that of a solvent molecule, the smallest entity in our system, the wave propagation speed continues to increase to an unrealistic value. Nevertheless, the simulations provide very important qualitative results: a stark change in the diffusion constant at the wave front, leading to the linear propagation of waves in time and sharp wave fronts. In fact, when $\Delta x = 10$ nm, $D_{wet} = 10^{-5}$ cm^2 s^{-1}, $D_{dry} = 10^{-10}$ cm^2 s^{-1}, and $\kappa = 30$, the simulated wave front propagates at a constant speed of 7 μm/s, which is comparable to the ECL wave speed observed in our experiments.

This ionic cluster model, particularly with respect to the rapid switch in the diffusion coefficient between the oxidized and non-oxidized polymer phases, indicates that EC oxidation takes place at the interface between the two phases. From a microscopic point of view, the diffusion of anions, holes, and solvent molecules into the non-oxidized polymer phase changes the properties of the polymer to facilitate further diffusion of these solutes. This self-promoting effect leads to the quick swelling and oxidation of the polymer. The interface expands isotropically because the diffusion of solutes is not directional within the plane parallel to the underlying ITO substrate, as demonstrated by the ECL rings observed.

CONCLUSIONS

The points of contact between the working electrodes, the polymer film, and the electrolyte solution are the triggering sites for the EC oxidation of F8BT films. Using electron-beam lithography to define precisely the positions of these triggering sites affords greater control in reproducing the ECL waves and therefore provides a reliable system for studying the observed oxidation phenomena. We have shown that the lateral propagation of the oxidized polymer phase in F8BT films results from a stark change in the diffusion coefficient of solutes between the oxidized and non-oxidized polymer phases. Moreover, diffusion is governed by the correlated motion of charged species and solvent molecules in the electrolyte and polymer that contribute to the ECL reactions and polymer swelling. These experiments have also provided a valuable springboard for exploring the effects of various processing parameters (electrolyte concentration, co-reactant concentration, anionic species, etc.) on ECL wave initiation and propagation, especially as they contribute to the further development of the physical model for oxidation in conjugated polymers herein described. This new perspective on EC oxidation kinetics may also be extended to many polymer systems other than the one studied here and is of fundamental importance to both electrochemistry and polymer science.

ASSOCIATED CONTENT

Supporting Information. Appendix I, ECL movies (AVI), and additional supporting data. This material is available free of charge via the Internet at http://pubs.acs.org.

AUTHOR INFORMATION

Corresponding Author
sguo40@mail.gatech.edu.

Notes

[‖] Professor Paul F. Barbara passed away Oct 31, 2010.

ACKNOWLEDGMENT

This work was supported by the National Science Foundation (CHE-0717998) and the Welch Foundation. O.F. was supported by a National Science Foundation IGERT Grant (DGE-0549417). The authors thank Dr. Keith J. Stevenson and Dr. Joshua C. Bolinger for helpful discussions and critical comments on the manuscript.

REFERENCES

(1) Armstrong, N. R.; Wightman, R. M.; Gross, E. M. *Annu. Rev. Phys. Chem.* **2001**, *52*, 391.
(2) Adhikari, B.; Majumdar, S. *Prog. Polym. Sci.* **2004**, *29*, 699.
(3) Wang, L.; Fine, D.; Sharma, D.; Torsi, L.; Dodabalapur, A. *Anal. Bioanal. Chem.* **2006**, *384*, 310.
(4) Heuer, H. W.; Wehrmann, R.; Kirchmeyer, S. *Adv. Funct. Mater.* **2002**, *12*, 89.
(5) Rauh, R. D. *Electrochim. Acta* **1999**, *44*, 3165.
(6) Jager, E. W. H.; Smela, E.; Inganas, O. *Science* **2000**, *290*, 1540.
(7) Smela, E. *Adv. Mater.* **2003**, *15*, 481.
(8) Tezuka, Y.; Aoki, K.; Ishii, A. *Electrochim. Acta* **1999**, *44*, 1871.
(9) Tezuka, Y.; Kimura, T.; Ishii, T.; Aoki, K. *J. Electroanal. Chem.* **1995**, *395*, 51.
(10) Tezuka, Y.; Ohyama, S.; Ishii, T.; Aoki, K. *Bull. Chem. Soc. Jpn.* **1991**, *64*, 2045.
(11) Wang, X. Z.; Shapiro, B.; Smela, E. *Adv. Mater.* **2004**, *16*, 1605.
(12) Wang, X. Z.; Shapiro, B.; Smela, E. *J. Phys. Chem. C* **2009**, *113*, 382.
(13) Wang, X. Z.; Smela, E. *J. Phys. Chem. C* **2009**, *113*, 359.
(14) Wang, X. Z.; Smela, E. *J. Phys. Chem. C* **2009**, *113*, 369.
(15) West, B. J.; Otero, T. F.; Shapiro, B.; Smela, E. *J. Phys. Chem. B* **2009**, *113*, 1277.
(16) Otero, T. F.; Boyano, I. *J. Phys. Chem. B* **2003**, *107*, 6730.
(17) Otero, T. F.; Grande, H.; Rodriguez, J. *J. Phys. Org. Chem.* **1996**, *9*, 381.
(18) Otero, T. F.; Grande, H.; Rodriguez, J. *J. Phys. Chem. B* **1997**, *101*, 8525.
(19) Otero, T. F.; Grande, H.; Rodriguez, J. *J. Phys. Chem. B* **1997**, *101*, 3688.
(20) Richter, M. M. *Chem. Rev.* **2004**, *104*, 3003.
(21) Chang, Y. L.; Palacios, R. E.; Fan, F. R. F.; Bard, A. J.; Barbara, P. F. *J. Am. Chem. Soc.* **2008**, *130*, 8906.
(22) Chang, Y. L.; Palacios, R. E.; Chen, J. T.; Stevenson, K. J.; Guo, S.; Lackowski, W. M.; Barbara, P. F. *J. Am. Chem. Soc.* **2009**, *131*, 14166.
(23) Kaufman, F. B.; Schroeder, A. H.; Engler, E. M.; Kramer, S. R.; Chambers, J. Q. *J. Am. Chem. Soc.* **1980**, *102*, 483.
(24) Bertoncello, P.; Forster, R. J. *Biosens. Bioelectron.* **2009**, *24*, 3191.
(25) Forster, R. J.; Bertoncello, P.; Keyes, T. E. *Annu. Rev. Anal. Chem.* **2009**, *2*, 359.
(26) Richter, M. M.; Fan, F. R. F.; Klavetter, F.; Heeger, A. J.; Bard, A. J. *Chem. Phys. Lett.* **1994**, *226*, 115.
(27) Zhang, X. J.; Jenekhe, S. A. *Macromolecules* **2000**, *33*, 2069.
(28) Lacroix, J. C.; Fraoua, K.; Lacaze, P. C. *J. Electroanal. Chem.* **1998**, *444*, 83.
(29) Edwards, D. A. *SIAM J. Appl. Math.* **1995**, *55*, 1039.
(30) Edwards, D. A.; Cohen, D. S. *SIAM J. Appl. Math.* **1995**, *55*, 662.